Sukarno, Cheryl Suwen Law and Abel Santos
**Realisation and optical engineering of linear variable bandpass filters in nanoporous anodic alumina photonic crystals**
Nanoscale, 2017; 9(22):7541-7550



Published at: http://dx.doi.org/10.1039/C7NR02115A

Nanoscale

Accepted Manuscript

This article can be cited before page numbers have been issued, to do this please use: S. Sukarno, C. S. Law and A. Santos, *Nanoscale*, 2017, DOI: 10.1039/C7NR02115A.

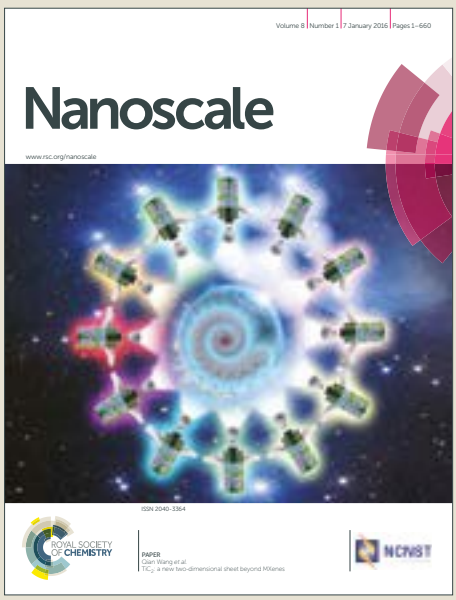




ROYAL SOCIETY OF CHEMISTRY

rsc.li/nanoscale

View Article Online
DOI: 10.1039/C7NR02115A

Nanoscale

PAPER

# Realisation and optical engineering of linear variable bandpass filters in nanoporous anodic alumina photonic crystals

Received 00th January 2017,
Accepted 00th January 2017

DOI: 10.1039/x0xx00000x

www.rsc.org/

Sukarno[a], Cheryl Suwen Law[a,b,c], and Abel Santos[*a,b,c]

We present the first realisation of linear variable bandpass filters in nanoporous anodic alumina (NAA-LVBPFs) photonic crystal structures. NAA gradient-index filters (NAA-GIFs) are produced by sinusoidal pulse anodisation and used as photonic crystal platforms to produce NAA-LVBPFs. The anodisation period of NAA-GIFs is modified from 650 to 850 s to systematically tune the characteristic photonic stopband of these photonic crystals across the UV-visible-NIR spectrum. Then, the nanoporous structure of NAA-GIFs is gradually widened along the surface under controlled conditions by wet chemical etching using a dip coating approach aiming to create NAA-LVBPFs with finely engineered optical properties. We demonstrate that the characteristic photonic stopband and the iridiscent interferometric colour displayed by these photonic crystals can be tuned with precision across the surface of NAA-LVBPFs by adjusting the fabrication and etching conditions. Here, we envisage for the first time the combination of anodisation period and etching conditions as a cost-competitive, facile, and versatile nanofabrication approach that enables the generation of a broad range of unique LVBPFs covering the spectral regions. These photonic crystal structures open new opportunities for multiple applications, including adaptive optics, hyperspectral imaging, fluorescence diagnostics, spectroscopy, and sensing.

## Introduction

To filter light – i.e. to selectively transmit or reflect light of specific wavelengths or wavelength ranges – is a critical functionality for a broad range of optoelectronic and photonic devices and applications such as telecommunications, spectroscopy, imaging, lasers, diagnosis and medical therapies.[1-3] Optical filters can provide a precise control over electromagnetic waves by allowing and/or forbidding the pass of photons of certain energy/wavelength, enabling the fine control of light for specific applications.[4,5] Generally, optical filters are based on glass or plastic matrices, the optical properties of which are engineered by additional inorganic or organic coatings that enable the control and tuneability of the filtering features of the filter (e.g. width and position of photonic bands, cut-off and cut-on wavelengths, etc.).

Among the broad variety of optical filters, linear variable bandpass filters (LVBPFs) have photonic bands with variable central wavelength, the position of which is shifted across the surface of the filter in a linear fashion.[6-8] Typically, LVBPFs are produced by interference coatings intentionally wedged in one direction across the surface of the filter.[9-11] LVBPFs can be fabricated by deposition and dry etching[9], deposition and masking[10], and combinational etching[11]. The optical properties of LVBPFs can be controlled by the deposition conditions such as the angle of the substrate with respect to the deposition target, deposition time and temperature, masking approach, and etching conditions. These fabrication techniques make it possible to fabricate LVBPFs that can cover the broad range of spectral regions, from UV to IR. Furthermore, the blocking and transmission bands can be adjusted by reorienting the filter to the light source, opening many possibilities to filter light for specific applications.

However, LVBPFs are not limited to traditional fabrication processes and materials. For instance, Sailor and others demonstrated the generation of LVBPFs in porous silicon (pSi) by direct electrochemical etching using an asymmetric electrode configuration, where the cathode is displaced from the centre of the silicon substrate during the etching process.[12-16] The optical properties of pSi-LVBPFs were demonstrated to be tuneable by means of the fabrication conditions such as the acid electrolyte concentration, the etching current density, and the position of the cathode relative to the silicon substrate surface since these parameters establish the geometric characteristics of the pSi film (i.e. thickness, porosity, and pore size). These pSi-LVBPFs were demonstrated as nanoporous photonic platforms for developing size-exclusion filters to establish the size of proteins[12], and visual sensors for organic solvents[15].

Nanoporous anodic alumina (NAA) has long been considered a promising platform for the development of photonic crystal structures due to its optical and geometric characteristics.[17] NAA is produced by anodisation of aluminium in acid electrolytes and its nanoporous structure, composed of

[a] School of Chemical Engineering, The University of Adelaide, Engineering North Building, 5005 Adelaide, Australia.
[b] Institute for Photonics and Advanced Sensing (IPAS), The University of Adelaide, 5005 Adelaide, Australia.
[c] ARC Centre of Excellence for Nanoscale BioPhotonics (CNBP), The University of Adelaide, 5005 Adelaide, Australia.
* E-Mail: abel.santos@adelaide.edu.au

View Article Online
DOI: 10.1039/C7NR02115A




cylindrical nanopores, can be precisely engineered by different approaches.[18-22] Pioneering studies revealed that 2D NAA photonic crystals featuring straight cylindrical nanopores present a photonic stopband, the characteristics of which rely on the geometric features of the NAA matrix (e.g. chemical composition, lattice constant, filling factor).[23-25] Recently, structural engineering approaches have enabled the generation of a series of innovative multi-dimensional NAA-based photonic crystal structures such as Fabry-Pérot interferometers, microcavities, bandpass filters, gradient-index filters, distributed Bragg reflectors, etc.[26-36] These fabrication approaches make it possible the modulation of the effective refractive index of NAA in depth, opening new paths for the precise engineering of photonic structures.

However, the effective medium of NAA can also be engineered in the perpendicular direction to its nanopores. For instance, Wang *et al.* used an etching approach to create lateral nanopore size gradients on NAA substrates featuring straight cylindrical nanopores from top to bottom.[37] These substrates were then used as supports to study the growth and differentiation of human mesenchymal stem cells over different nanotopographies. Another study by Kant *et al.* created NAA layers displaying nanopore gradients along the surface by a so-called "nonlinear anodisation", where cathode and anode are angled $45^0$ each other.[38] Although the authors observed the generation of iridescence phenomenon in the resulting films, the controllability of the method was not demonstrated. The resulting films, which featured wire-like alumina in over-etched sections, were assessed as substrates for the growth of neuroblastoma cells.

In this study, we present a facile synthesis approach to produce a new generation of LVBPFs based on NAA with versatile and controlled optical filtering features by combining anodisation and chemical etching. Firstly, we fabricate a set of NAA-GIFs with different period lengths by sinusoidal pulse anodisation of aluminium (**Fig. 1a**). The nanoporous structure of these NAA-GIFs is selectively widened by wet chemical etching under controlled conditions through a dip coating approach (**Fig. 1b**). This process is performed so the nanopore diameter is linearly widened across the surface of these photonic crystal structures (**Fig. 1c**). The optical filtering features of these NAA-GIFs can be finely tuned due to the dependence of the photonic stopband of NAA-GIFs with their nanoporous structure, resulting in a set of unique NAA-LVBPFs.

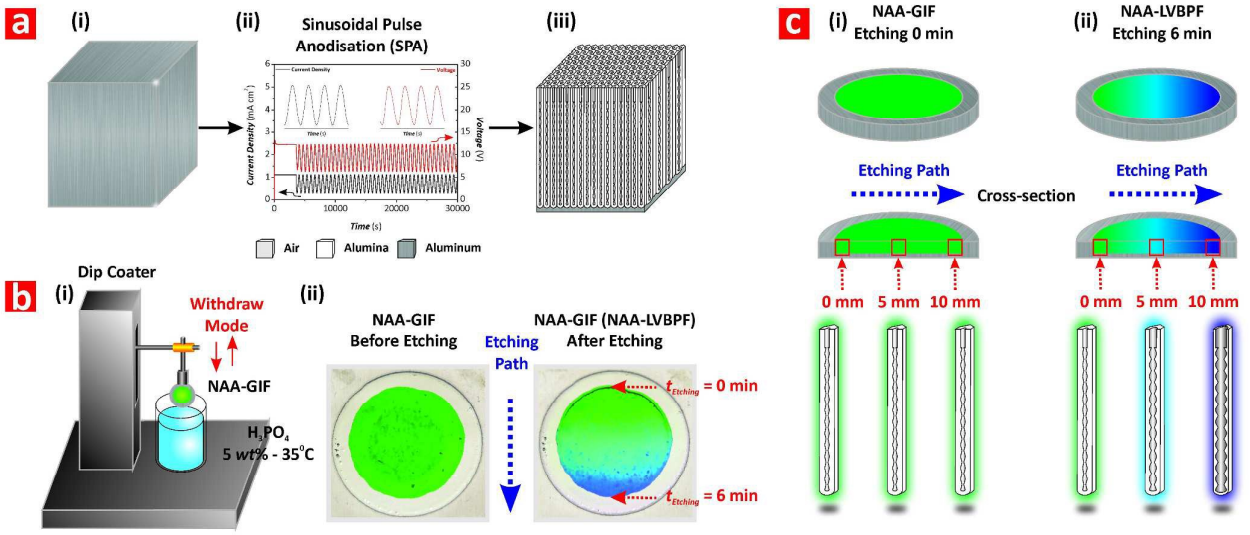


**Fig. 1** Fabrication of NAA-LVBPFs by controlled wet chemical etching of NAA-GIFs produced by sinusoidal pulse anodisation. a) Production of NAA-GIFs by SPA: (i) aluminium substrate, (ii) representative anodisation profile, and (iii) structure of NAA-GIFs. b) Generation of NAA-LVBPFs from NAA-GIFs by dip coating approach: (i) illustration showing details of the dip coater system used to produce NAA-LVBPFs in an aqueous solution of $H_3PO_4$ 5 *wt*% at $35^0$C, and (ii) digital images showing the structure of NAA-GIF before (left) and after (right) asymmetrical chemical etching along the etching path (NB: NAA-GIF produced with $T_p$ = 650 s, $A_J$ = 0.420 mA cm$^{-2}$, $J_{Off}$ = 0.280 mA cm$^{-2}$, $t_{SPA}$ = 20 h, $T_{an}$ = -1°C and $t_{Etching}$ = 6 min). c) Details of the relationship existing between the interferometric colour and the nanoporous structure of NAA-GIFs before (i) and after (ii) chemical etching (top – NAA chip, centre – cross-sectional view of NAA chip at specific positions, and bottom – nanopore geometry at specific positions following the etching path along the surface of NAA-GIFs).

## Experimental

### Materials

NAA-GIFs were fabricated by anodising high purity aluminium (Al) substrates (99.9997%), 320 μm thick, provided by Goodfellow Cambridge Ltd. (UK). Sulphuric acid ($H_2SO_4$), hydrochloric acid (HCl), perchloric acid ($HClO_4$), copper(II) chloride ($CuCl_2$), and phosphoric acid ($H_3PO_4$) were provided by Sigma-Aldrich (Australia) and ethanol (EtOH – $C_2H_5OH$) was purchased from ChemSupply (Australia). All the chemicals used in this study were used as received, without further purification. Aqueous solutions were prepared in ultrapure water (18.2 MΩ·cm) Option Q–Purelabs (Australia).

### Fabrication of NAA-GIFs by sinusoidal pulse anodisation



 

View Article Online
DOI: 10.1039/C7NR02115A





NAA-GIFs were fabricated by sinusoidal pulse anodisation (SPA) under galvanostatic conditions following the process reported elsewhere.[35,39] Prior to anodisation, 2.25 $cm^2$ square Al chips were sonicated in ethanol and water sequentially for 15 min each. Then, Al chips were electrochemically polished in a mixture composed of EtOH:$HClO_4$ 4:1 (*v*:*v*) at 20 V and 5°C for 3 min. Electropolished Al chips displayed a mirror-like finishing, denoting a smooth surface at nanometric scale. Once electropolished, Al chips were anodised by SPA in an aqueous electrolyte solution 1.1 M $H_2SO_4$ modified with 25 *v*% EtOH to prevent it from freezing.[40,41] The temperature of the electrolyte solution ($T_{an}$) was kept at -1°C throughout the anodisation process to overcome the dissolution of the oxide film. The SPA process started with an initial step at 1.120 mA $cm^{-2}$ for 1 h to achieve a homogeneous oxide growth rate. Then, the anodisation profile was set to SPA mode, where the anodising current density was pulsed between high ($J_{max}$ = 1.120 mA $cm^{-2}$) and low ($J_{min}$ = 0.280 mA $cm^{-2}$) values in a sinusoidal manner. The anodisation profiles were automatically generated by a Labview®-based software following **Eq. 1**:

$$J(t) = A_J \cdot \left[Sin\left(\frac{2\pi}{T_P} \cdot t\right) + 1\right] + J_{off} \quad (1)$$

where $J(t)$ is the current density at time $t$, $A_J$ is the current density amplitude, $T_P$ is the anodisation period, and $J_{off}$ is the current density offset.

The SPA time ($t_{SPA}$), $A_J$ and $J_{off}$ were fixed to 20 h, 0.420 mA $cm^{-2}$, and 0.280 mA $cm^{-2}$, respectively, and $T_P$ was systematically modified from 650 to 850 s, with a $\Delta T_P$ = 100 s.

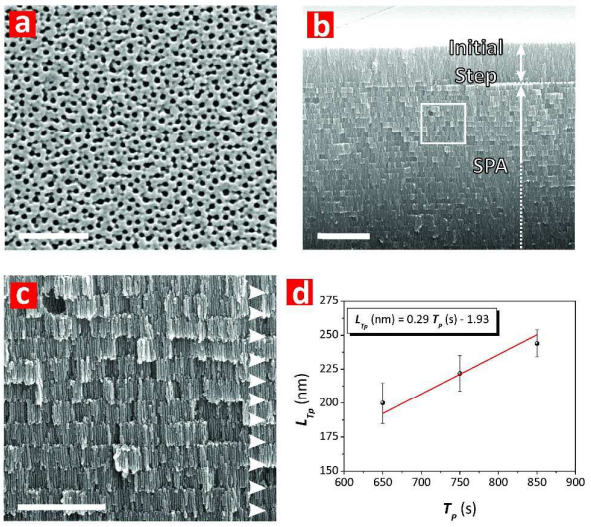


**Fig. 2** Representative SEM images of NAA-GIFs produced by SPA. a) Top view SEM image of a NAA-GIF produced with $T_p$ = 650 s, $A_J$ = 0.420 mA $cm^{-2}$, $J_{Off}$ = 0.280 mA $cm^{-2}$, $t_{SPA}$ = 20 h, $T_{an}$ = -1°C, and $t_{Etching}$ = 6 min (scale bar = 250 nm). b) Cross-sectional SEM image of a NAA-GIF showing details of the layered structure, including the layers produced during the initial anodisation step and the SPA section (scale bar = 2.5 µm). c) Magnified view of the white square shown in (b) (scale bar = 1 µm) (NB: white arrowheads identify the layers produced after each pulse during SPA). d) Fitting line establishing the linear relationship between anodisation period ($T_P$) and period length ($L_{Tp}$).

### Fabrication of NAA-LVBPFs by wet chemical etching of NAA-GIFs

A set of NAA-GIFs produced with different anodisation periods (i.e. 650, 750, and 850 s) were used as photonic crystal platforms to develop NAA-LVBPFs by wet chemical etching. In this process, the NAA-GIFs were fixed to the substrate holder of a dip coater to attain a precise control over the etching process along the surface of these photonic crystals. Then, NAA-GIFs were dipped into an aqueous solution $H_3PO_4$ 5 *wt*% at 35°C to etch/widen their nanoporous structure. After total immersion, the NAA-GIFs were progressively withdrawn from the solution at controlled speed by means of an automatic motorised stage. The withdraw speed was adjusted per the diameter of the NAA-GIFs (i.e. 10 mm) to modify the overall etching time ($t_{Etching}$) systematically from 0 to 10 min with a $\Delta t_{Etching}$ = 1 s. Just after etching, the NAA-LVBPFs were thoroughly washed with ultrapure water, carefully dried under air stream, and stored until further characterisation. **Table S1 (ESI)** includes a summary of the withdraw speeds for each $t_{Etching}$.

### Optical characterisation

The interferometric colour displayed by NAA-LVBPFs as a function of the anodisation period ($T_P$) and the etching time ($t_{Etching}$) was characterised by digital images acquired with a Canon EOS 700D digital camera equipped with a Tamron 90 mm F2.8 VC USD macro mount lens with autofocus function under natural illumination. Digital images were acquired at an angle of 10° with respect to the camera and with normal incidence of light. A schematic showing the configuration of our digital characterisation setup is shown in **Fig. S1** (**ESI**). The aluminium substrate in NAA-LVBPFs was removed from the backside by selective etching in a saturated solution of HCl/$CuCl_2$ using an etching cell with a circular window of 9 mm in diameter. Note that 1 mm of aluminium was left to give mechanical stability to NAA-LVBPFs for handling. A black card was used as a background for image purposes. The plugin 'Measure RGB' in ImageJ was employed to establish the RGB values of each NAA-LVBPF (public domain program developed at the RSB of the NIH).[42]

The position of the central wavelength of the photonic stopband ($\lambda_{C\text{-}PSB}$) of NAA-LVBPFs was established by reflection spectroscopy, using an optical fibre spectrometer, at normal incidence (i.e. $\theta$ = 0°). This system is composed of a tungsten source from which white light is directed onto the surface of NAA-LVBPFs by a bifurcated optical fibre probe. The illumination spot was adjusted to 2 mm by a collimating lens system (74-VIS, Ocean Optics, USA). Light reflected from the NAA-LVBPFs was collected by the optical probe and guided to an optical spectrometer (FLAME-T-VIS-NIR-ES, Ocean Optics,

View Article Online
DOI: 10.1039/C7NR02115A




USA). The reflection spectra were collected along the surface of NAA-LVBPFs at steps of 1 mm ($\Delta X_{NAA\text{-}LVBPF}$ = 1 mm), from $X_{NAA\text{-}LVBPF}$ = 0 to 10 mm) following the etching path by means of a micro-stage. The reflection spectra were acquired from 400 to 1000 nm with an integration time of 20 s and 20 average measurements. The position of the central wavelength was estimated in Igor Pro library (Wavemetrics, USA) by Gaussian fitting.

### Structural characterisation

The geometric features of nanopores in NAA-LVBPFs were characterised by a field emission gun scanning electron microscope (FEG-SEM FEI Quanta 450). FEG-SEM images were processed by ImageJ to estimate the average nanopore diameter ($d_P$) and period length ($L_{Tp}$) of the NAA-LVBPFs.[42]

## Results and discussion

### Structure of NAA-GIFs produced by SPA

As reported in our previous studies, NAA-GIFs produced by SPA feature a layered nanoporous structure.[35,39] **Fig. 2** compiles representative SEM images of NAA-GIFs produce by SPA under the conditions specified in our study. The top surface of these photonic crystal structures features nanopores randomly distributed since the fabrication conditions used in our study were out of the self-organisation regime (**Fig. 2a**). NAA-GIFs can be described as a stack of layers of NAA in which the diameter of its nanopores is sinusoidally modified in depth following the anodising current density profile (**Fig. 2b**). Arrowheads in **Fig. 2c** denote the interfaces between different layers in the structure of NAA-GIFs. The distance between adjacent layers is defined as the period length ($L_{Tp}$), which was found to follow a linear relationship with the anodisation period ($T_P$) (**Fig. 2d**). In our study, we modified $T_P$ from 650 to 850 s, with $\Delta T_P$ = 100 s, which corresponded to $L_{Tp}$ = 200 ± 15, 222 ± 13, and 244 ± 10 nm, respectively. A fitting confirms the linear correlation between anodisation period and period length in the structure of NAA-GIFs, which is in good agreement with previous studies.[35,39]

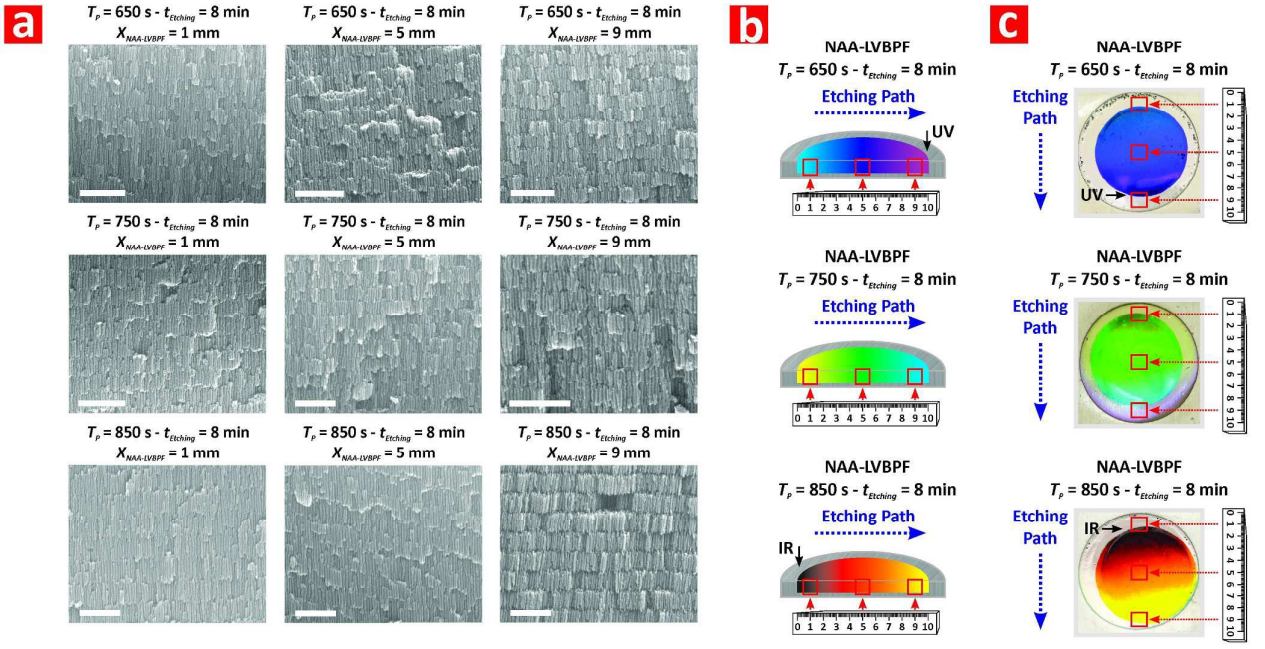


**Fig. 3** Structural characterisation of NAA-LVBPFs as a function of the anodisation period ($T_P$) and the etching path position ($X_{NAA\text{-}LVBPF}$). a) Cross-sectional SEM images acquired at different positions ($X_{NAA\text{-}LVBPF}$ = 1, 5, and 9 mm) of NAA-LVBPFs produced with $T_P$ = 650, 750, and 850 s (scale bars = 1 μm). b) Schematic illustrations of NAA-LVBPFs showing the position of the cross-sections where SEM images were acquired (top – $T_P$ = 650 s, middle – $T_P$ = 750 s, and bottom – $T_P$ = 850 s). c) Digital images of actual NAA-LVBPFs showing the position of SEM image acquisition along the etching path (top – $T_P$ = 650 s, middle – $T_P$ = 750 s, and bottom – $T_P$ = 850 s) (NB: the interferometric colour of these photonic crystals can be tuned from UV to IR by the anodisation period and the etching time).

### Structure of NAA-LVBPFs produced by etching of NAA-GIFs

As mentioned before, NAA-LVBPFs were produced by controlled etching of the structure of NAA-GIFs, using a dip coating approach, where the wet chemical etching process is controlled by the withdraw speed of NAA-GIFs from the etchant solution (5 *wt*% $H_3PO_4$ at 35°C). This fabrication method enables the fine tuning of the nanopore diameter along the surface of the NAA-LVBPFs. Those sections of the NAA-LVBPF exposed to the etching solution for longer time display wider nanopores in depth due to the anisotropic nature of alumina ($Al_2O_3$) etching in phosphoric acid.

Here, we envisage for the first time an innovative approach to generate a new class of linear variable bandpass filters based on NAA photonic crystals, the effective medium of



 

View Article Online
DOI: 10.1039/C7NR02115A





which is engineered laterally and in depth. This type of LVBPFs could provide advanced performances for multiple applications given that the filtering characteristics can be finely and broadly tuned by the fabrication and etching conditions. For instance, the filtering features of NAA-LVBPFs can be engineered across the spectral regions (i.e. from UV to IR) by means of the anodisation period and the withdraw speed during the anodisation and etching processes, respectively. Furthermore, the use of other NAA-based photonic crystal platforms (e.g. distributed Bragg reflectors, microcavities, bandpass filters, etc.)[17] with different photonic stopband features offers numerous paths to create a variety of NAA-LVBPFs with precisely engineered filtering properties for specific applications. Another unique property of NAA-LVBPFs is that their filtering features can be further tuned by modifying their effective medium, which could be readily used to develop LVBPFs with tuneable properties (e.g. infiltration with liquid crystals, photo-switchable molecules, etc.). In contrast with other fabrication approaches, the nanoporous structure of NAA-LVBPFs produced by this fabrication method does not display over-etched areas and keeps its original layered morphology, which is an aspect of paramount importance to attain a fine control over the optical properties of these photonic films.

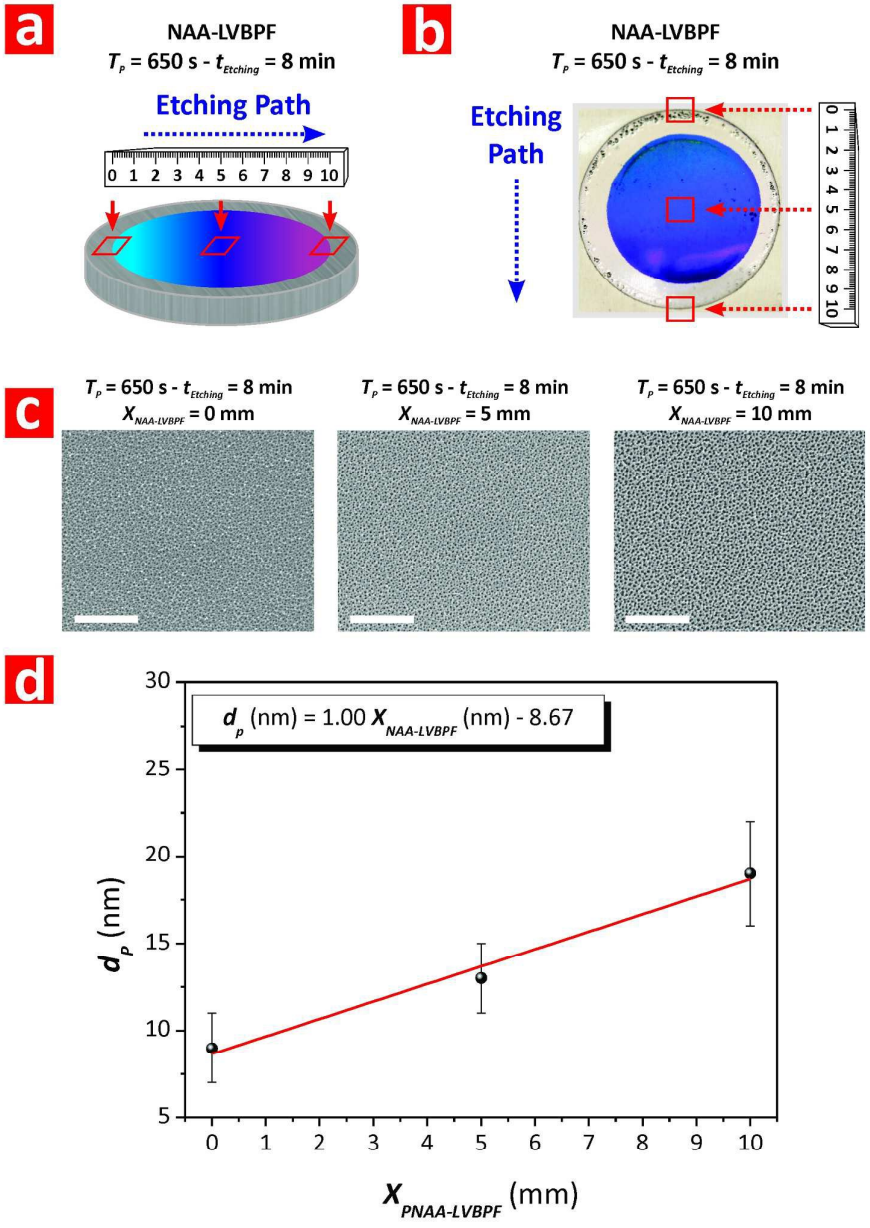


**Fig. 4** Structural characterisation of NAA-LVBPFs as a function of the anodisation period ($T_P$) and the positon along the etching path ($X_{NAA-LVBPF}$). a) Schematic of a NAA-LVBPFs produced with $T_P$ = 650 s and $t_{Etching}$ = 8 min showing the positions along the etching path where SEM images were acquired (top – $X_{NAA-LVBPF}$ = 0 mm, middle – $X_{NAA-LVBPF}$ = 5 mm, and bottom – $X_{NAA-LVBPF}$ = 10 mm). c) Digital image of a NAA-LVBPF produced with $T_P$ = 650 s and $t_{Etching}$ = 8 min showing

View Article Online
DOI: 10.1039/C7NR02115A


the position of acquisition along the etching path and its interferometric colour (top – $X_{NAA\text{-}LVBPF}$ = 0 mm, middle – $X_{NAA\text{-}LVBPF}$ = 5 mm, and bottom – $X_{NAA\text{-}LVBPF}$ = 10 mm). c) Top view SEM images acquired at different positions (top – $X_{NAA\text{-}LVBPF}$ = 0 mm, middle – $X_{NAA\text{-}LVBPF}$ = 5 mm, and bottom – $X_{NAA\text{-}LVBPF}$ = 10 mm) of a NAA-LVBPF produced with $T_P$ = 650 s and $t_{Etching}$ = 8 min (scale bars = 500 nm). d) Fitting line establishing the linear relationship between $d_P$ and $X_{NAA\text{-}LVBPF}$.

**Fig. 3** compiles a series of representative cross-sectional SEM images showing the structure of NAA-LVBPFs produced using NAA-GIFs fabricated with $T_P$ 650, 750, and 850 s for $t_{Etching}$ = 8 min. As these cross-sectional images reveal, the structure of the original NAA-GIFs is progressively widened along the etching path. The diameter of the nanopores becomes wider as $X_{NAA\text{-}LVBPF}$ varies from 0 to 10 mm. **Fig. 3a** shows the characteristic layered structure of NAA-GIFs, where the nanopore diameter is widened at different positions of the photonic crystal structure (i.e. at $X_{NAA\text{-}LVBPF}$ = 1, 5, and 9 mm) to form NAA-LVBPFs with different period lengths as per the anodisation period used during the fabrication of NAA-GIFs ($T_P$ = 650, 750, and 850 s). **Fig. 3b** shows an illustration depicting the characterisation process of NAA-LVBPFs, from where cross-sectional SEM images were acquired. As digital images of these photonic crystal structures show (**Fig. 3c**), the reflection of NAA-LVBPFs can be precisely tuned from UV to IR (**Figs. 3b and c**). The iridescent interferometric colour displayed by these photonic crystals can be tuned from UV to IR throughout the visible region. NAA-LVBPFs were found to display vivid purple, blue, cyan, green, chartreuse, yellow, orange, and red colour. Note that the reflection of NAA-LVBPFs undergoes a blue shift with the etching path as the nanoporous structure is widened, which is in good agreement with previous studies.[43-50]

**Figs. 4a and b** show a visual description of the positions at which SEM images were acquired along the etching path of NAA-LVBPFs. Top SEM images of a representative NAA-LVBPF structure produced with $T_P$ = 650 s and $t_{Etching}$ = 8 min denote an increasing nanopore diameter ($d_P$) with the etching path (**Fig. 4c**). Image analysis was used to establish the nanopore diameter as a function of the position along the etching path. The obtained results demonstrate that at $X_{NAA\text{-}LVBPF}$ = 0, 5, and 10 mm, the NAA-LVBPF features $d_p$ = 9 ± 2, 13 ± 2, and 19 ± 3 nm, respectively (**Fig. 4d**). We found a linear dependence of $d_P$ with $X_{NAA\text{-}LVBPF}$ along the etching path, which is an indication of the accuracy and controllability of the proposed fabrication process to produce linear variable optical filters.

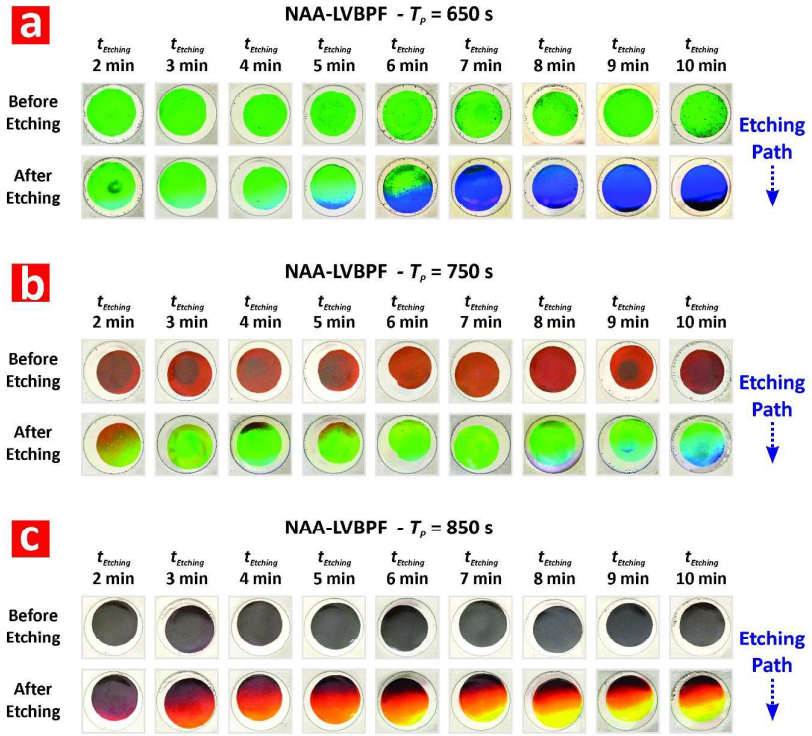


**Fig. 5** Tuning of interferometric colour in NAA-LVBPFs (NB: the black colour displayed in NAA-LVBPFs produced with $T_P$ = 650 s at $t_{Etching}$ = 8, 9, and 10 min, and $T_P$ = 850 s at $t_{Etching}$ = 0-10 min corresponds to the UV and IR regions, respectively). a) Digital images of NAA-LVBPFs produced with $T_P$ = 650 s before and after etching at different etching times (from $t_{Etching}$ = 2 to 10 min). b) Digital images of NAA-LVBPFs produced with $T_P$ = 750 s before and after etching at different etching times (from $t_{Etching}$ = 2 to 10 min). c) Digital images of NAA-LVBPFs produced with $T_P$ = 850 s before and after etching at different etching times (from $t_{Etching}$ = 2 to 10 min).

**Characterisation and analysis of colour gradient in NAA-LVBPFs**

**Fig. 5** compiles a set of digital images of NAA-LVBPFs produced with anodisation period from 650 to 850 s and $t_{Etching}$ from 2 to 10 min. The interferometric colour displayed by NAA-LVBFs varies gradually along the etching path because of

View Article Online
DOI: 10.1039/C7NR02115A





the chemical etching process performed under controlled conditions. This property denotes the selective and asymmetric reflection of light across the spectral regions, from UV to IR, by these photonic crystal structures following the etching path. Among other fabrication parameters, it is well known that the central wavelength of the photonic stopband ($\lambda_{c\text{-}PSB}$) of NAA-based photonic crystal structures produced by pulse-like anodisation is directly dependent on the anodisation period ($T_P$) and the etching time ($t_{Etching}$).[35,39] As such, while the initial $\lambda_{c\text{-}PSB}$ ($\lambda_{c\text{-}PSB}$ at $t_{Etching}$ = 0 min) is established by the anodisation period used to produce the original NAA-GIF structure, this can be finely blue-shifted along the etching path by our fabrication approach. For instance, the original interferometric colour displayed by NAA-GIFs produced at $T_P$ = 650, 750, and 850 s is green, red, and black (i.e. transparent – IR), respectively (**Figs. 5a-c**). After etching, the original colour of these NAA-GIFs undergoes a progressive blue shift along the etching path, the magnitude of which is directly proportional to the total etching time. This results in the generation of a broad range of NAA-LVBPFs with precisely engineered filtering properties that can be tuned within the spectral regions by modifying $T_P$ and $t_{Etching}$ (**Figs. 5a-c**).

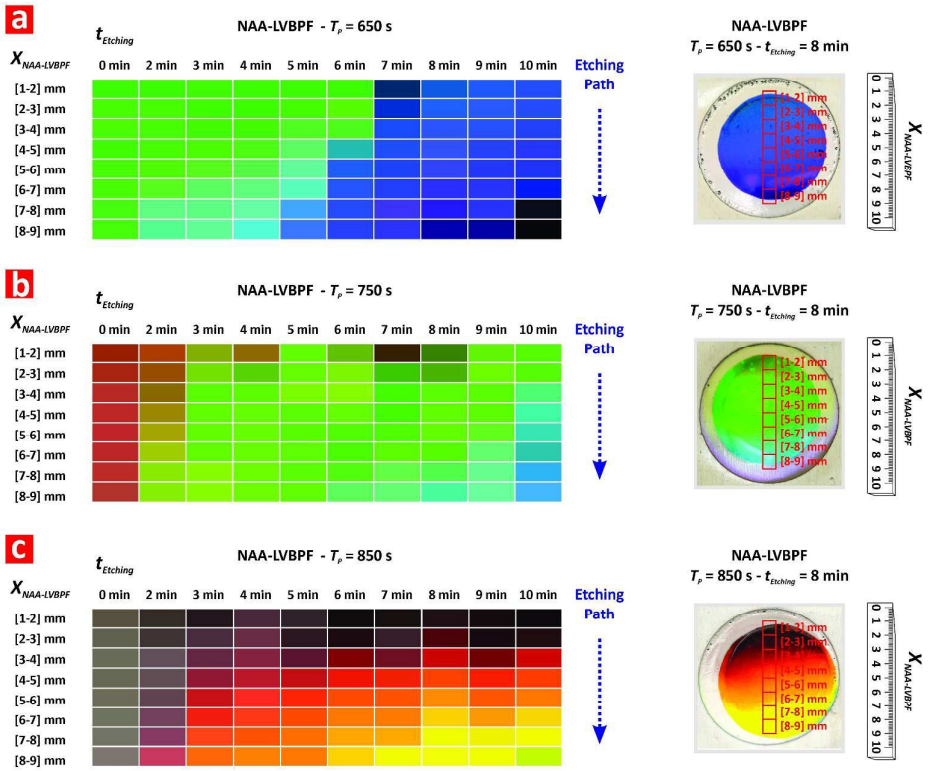


**Fig. 6** Colour map at different areas of NAA-LVBPFs as a function of the anodisation period ($T_P$) and the etching time ($t_{Etching}$). a) Colour map for NAA-LVBPFs produced with $T_P$ = 650 s for $X_{NAA\text{-}LVBPF}$ from [1-2] to [8-9] mm and $t_{Etching}$ from 0 to 10 min (left), and representative digital image showing the area positions across the surface of NAA-LVBFs over which image analysis was performed (right). b) Colour map for NAA-LVBPFs produced with $T_P$ = 750 s for $X_{NAA\text{-}LVBPF}$ from [1-2] to [8-9] mm and $t_{Etching}$ from 0 to 10 min (left), and representative digital image showing the area positions across the surface of NAA-LVBFs over which image analysis was performed (right). c) Colour map for NAA-LVBPFs produced with $T_P$ = 850 s for $X_{NAA\text{-}LVBPF}$ from [1-2] to [8-9] mm and $t_{Etching}$ from 0 to 10 min (left), and representative digital image showing the area positions across the surface of NAA-LVBFs over which image analysis was performed (right).

To gain a deeper understanding about the effect of $T_P$ and $t_{Etching}$ on the interferometric colour of NAA-LVBPFs, we performed systematic image analysis at the different areas of the digital images of NAA-LVBPFs shown in **Fig. 5**. **Figs. 6a-c** show colour maps obtained after analysing areas of 1 $mm^2$ (i.e. red squares shown in **Figs. 6a-c**) along the etching path. Image analysis was performed over the selected areas and the interferometric colour displayed by NAA-LVBPFs in these images was decomposed into average RBG values using ImageJ. A summary of the obtained results is presented in **Table S2** (**ESI**). This analysis denotes that the spatial dependence of the interferometric colour across the etching path of the different NAA-LVBPFs produced in this study is certainly controllable. It is observed how the original colour displayed by these photonic crystals is progressively blue-shifted with the etching time at the analysed areas. For instance, the initial colour of NAA-LVBPFs produced with $T_P$ = 650 s is green (19,194,65) at the top section of the filter ($t_{Etching}$ = 0 min; $X_{NAA\text{-}LVBPF}$ = [1-2] mm). However, the interferometric colour of these NAA-LVBPFs turns into blue (18,81,253) with the etching time ($t_{Etching}$ = 10 min; $X_{NAA\text{-}LVBPF}$ = [1-2] mm). NAA-LVBPFs fabricated with an anodisation period of 750 s display

View Article Online
DOI: 10.1039/C7NR02115A


red colour (162,74,53) before etching ($t_{Etching}$ = 0 min; $X_{NAA\text{-}LVBPF}$ = [1-2] mm), which becomes green (18,246,35) as the etching time increases ($t_{Etching}$ = 10 min; $X_{NAA\text{-}LVBPF}$ = [1-2] mm). Before etching, NAA-LVBPFs produced with $T_P$ = 850 s are transparent at any section of the filter (i.e. black colour due to the card used as a background during image acquisition), denoting that these photonic structures reflect light in the near IR region. However, vivid interferometric colours are observed with the etching time, becoming for example orange (251,101,15) at $t_{Etching}$ = 10 min and $X_{NAA\text{-}LVBPF}$ = [4-5] mm.

In summary, image analysis further evidences the controllability of the proposed approach to generate linear variable bandpass filters based on NAA.

### Tuneability of photonic stopband in NAA-LVBPFs

**Fig. 7** shows an example of tuneability of the position of the central wavelength of the photonic stopband ($\lambda_{C\text{-}PSB}$) in a NAA-LVBPF produced with $T_P$ = 750 s and $t_{Etching}$ = 4 min. As demonstrated in **Figs. 5 and 6**, the iridescent interferometric colour displayed by these photonic crystals along the etching path denotes a selective reflection of light across the surface of the filters (**Fig. 7a**). In this example, while $\lambda_{C\text{-}PSB}$ is located at 596 ± 1 nm at $X_{NAA\text{-}LVBPF}$ = 2 mm, this undergoes a linear blue shift along the surface of the NAA-LVBPF following the etching path, becoming 589 ± 1, 583 ± 1, 576 ± 1, and 566 ± 1 nm at $X_{NAA\text{-}LVBPF}$ = 3.5, 5.0, 6.5, and 8.0 mm, respectively (**Fig. 7b**).

It is worthwhile nothing that the full width at half maximum of the photonic stopband of NAA-LVBPFs ($FWHM_{PSB}$) was found to increase with the anodisation period and the etching time (**Fig. S2 – ESI**), from $T_P$ = 650 to 850 s and from $t_{Etching}$ = 0 to 6 min. $FWHM_{PSB}$ changes broadly within this range of fabrication parameters, from 19 ± 3 nm to 118 ± 10 nm, and the effect of the etching time had a more significant effect on this filtering feature than that of the anodisation period, as indicated by **Fig. S2 – ESI**.

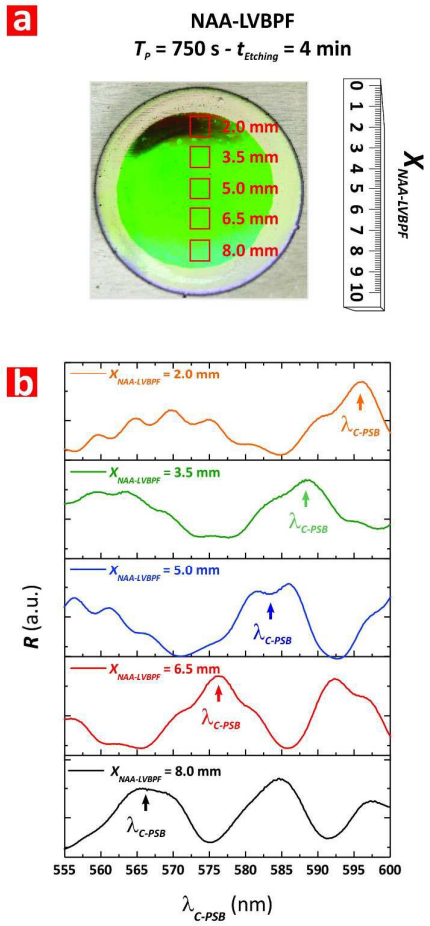


**Fig. 7** Characterisation of the position of the central wavelength of the photonic stopband ($\lambda_{C\text{-}PSB}$) of NAA-LVBPFs by reflection spectroscopy. a) Representative digital picture of a NAA-LVBPF produced with $T_P$ = 750 s and $t_{Etching}$ = 4 min (NB: red squares denote the position of the areas at which the reflection spectra in (b) were acquired – 2.0, 3.5, 5.0, 6.5, and 8.0 mm). b) Reflection spectra at different positions of the NAA-LVBPF shown in (a) (NB: arrows denote the position of the central wavelength, which is blue-shifted along the etching path).

View Article Online
DOI: 10.1039/C7NR02115A





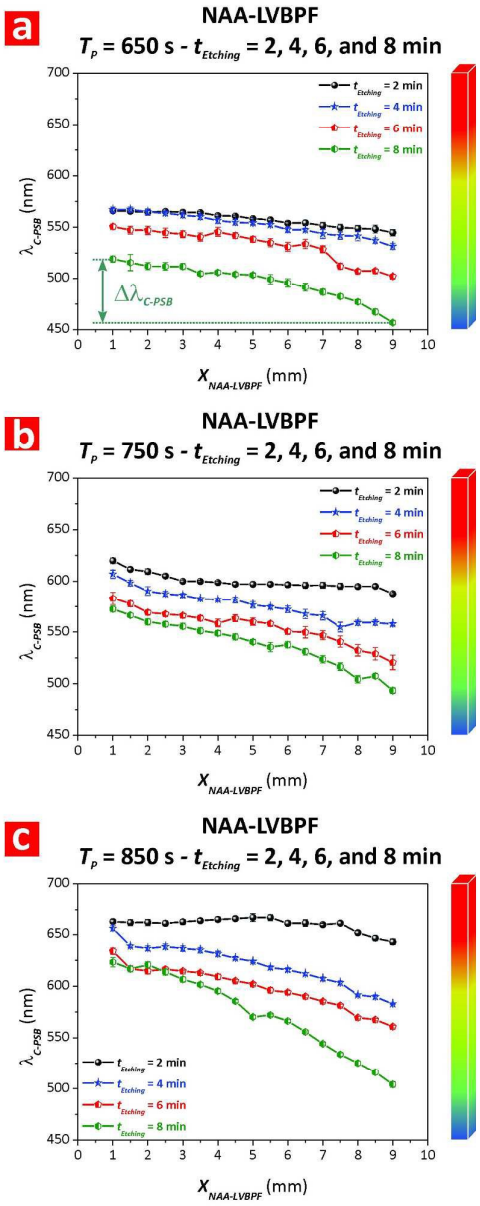


**Fig. 8** Tuneability of the position of the central wavelength in NAA-LVBPFs as a function of the anodisation period ($T_P$) and the etching time ($t_{Etching}$). a-c) Position of the central wavelength ($\lambda_{C\text{-}PSB}$) at different $X_{NAA\text{-}LVBPF}$ (i.e. from 1 to 9 mm with $\Delta X_{NAA\text{-}LVBPF}$ = 1 mm) for NAA-LVBPFs produced with $T_P$ = 650 (a), 750 (b), and 850 s (c) and $t_{Etching}$ = 2, 4, 6, and 8 min (NB: (a) includes a graphical definition of $\Delta\lambda_{C\text{-}PSB}$).

A fully extended analysis of the dependence of $\lambda_{C\text{-}PSB}$ with $X_{NAA\text{-}LVBPF}$ for the NAA-LVBPFs produced in our study is shown in **Fig. 8**. At first glance, it is observed that the position of the central wavelength is blue-shifted along the etching path as $X_{NAA\text{-}LVBPF}$ increases for NAA-LVBPFs produced with 650, 750, and 850 s (**Figs. 8a-c**, respectively). This blue shift was found to increase linearly with $t_{Etching}$. **Table 1** summarises the central wavelength shift ($\Delta\lambda_{C\text{-}PSB}$), defined as $\Delta\lambda_{C\text{-}PSB}$ = $\lambda_{C\text{-}PSB}$ at $X_{NAA\text{-}LVBPF}$ = 1 mm - $\lambda_{C\text{-}PSB}$ at $X_{NAA\text{-}LVBPF}$ = 9 mm, for NAA-LVBPFs produced with $T_P$ = 650, 750, and 850 s and $t_{Etching}$ = 2, 4, 6, and 8 min. A linear fitting of these values is shown in **Fig. S3 and Table S3 (ESI)**, indicating that $\Delta\lambda_{C\text{-}PSB}$ increases linearly with $t_{Etching}$ at any $T_P$. The slope of these linear fittings reveals that this blue shift increases with the anodisation period, being 7.4 ± 0.3, 7.7 ± 0.3, and 15.5 ± 2.8 nm min$^{-1}$, for $T_P$ = 650, 750, and 850 s, respectively. This analysis establishes that $\Delta\lambda_{C\text{-}PSB}$ is more marked for longer anodisation periods. Our analysis also established that the position of the central wavelength of the characteristic photonic stopband of NAA-LVBPFs can be linearly modified with high precision, as indicated by the values of $R^2$ shown in **Table S3 (ESI)**.

**Table 1** Summary of the dependence of the central wavelength shift ($\Delta\lambda_{C\text{-}PSB}$) with the anodisation period ($T_P$) and the etching time ($t_{Etching}$) for the NAA-LVBPFs fabricated in our study.

| $T_P$ (s) | $t_{Etching}$ (min) | $\Delta\lambda_{C\text{-}PSB}$ (nm) |
|---|---|---|
| 650 | 2 | 19 ± 2 |
| | 4 | 35 ± 3 |
| | 6 | 50 ± 4 |
| | 8 | 62 ± 4 |
| 750 | 2 | 32 ± 3 |
| | 4 | 49 ± 5 |
| | 6 | 62 ± 3 |
| | 8 | 79 ± 2 |
| 650 | 2 | 21 ± 2 |
| | 4 | 63 ± 3 |
| | 6 | 74 ± 5 |
| | 8 | 119 ± 6 |

## Conclusions

To summarise, we have developed a facile fabrication approach that enables for the first time the generation of precisely engineered linear variable bandpass filters based on nanoporous anodic alumina photonic crystals. NAA-GIFs produced with anodisation period from 650 to 850 s were used as photonic crystal platforms to develop NAA-LVBPFs with finely tuned filtering features covering the spectral regions, from UV to IR. In this process, the nanoporous structure of NAA-GIFs is chemically etched along the surface of these photonic crystals in a gradient-like fashion by dip coating in phosphoric acid etchant solution at a controlled temperature. During etching, the nanopores of NAA-GIFs are widened progressively along the etching path. Thus, the position of the characteristic photonic stopband of these filters is blue-shifted. The combination of anodisation period and withdraw speed during etching enables the fine tuning of the filtering features across the surface of NAA-LVBPFs. The optical properties of NAA-LVBPFs were characterised systematically by different techniques. These photonic crystal structures displayed vivid iridescent colours when reflecting light within

View Article Online
DOI: 10.1039/C7NR02115A




the visible spectrum, which can be readily tuned by the fabrication parameters (i.e. anodisation period and withdraw speed). The position of the photonic stopband of these optical filters along the etching path was characterised by reflection spectroscopy, revealing a strong linear relationship between $t_{Etching}$ and $\lambda_{C\text{-}PSB}$ at any anodisation period. This result is a clear evidence of the precision of our fabrication method to generate linear variable bandpass filters based on nanoporous anodic alumina. These photonic crystal structures could find broad applicability in adaptive optics, sensing and other applications.

## Acknowledgements

Support provided by the Australian Research Council (ARC) (DE140100549 and CE140100003), the University of Adelaide (UoA), the School of Chemical Engineering, the Institute for Photonics and Advanced Sensing (IPAS), and the ARC Centre of Excellence for Nanoscale BioPhotonics (CNBP). The Authors acknowledge the Adelaide Microscopy (AM) centre for FEG-SEM characterisation.

1 V. R. Supradeepa, C. M. Long, R. Wu, F. Ferdous, E. Hamidi, D. E. Leaird and A. M. Weiner, *Nat. Photonics*, 2012, **6**, 186.
2 M. Kues, C. Reimer, B. Wetzel, P. Roztocki, B. E. Little, S. T. Chu, T. Hansson, E. A. Viktorov, D. J. Moss and R. Morandotti, *Nat. Photonics*, 2017, **11**, 159.
3 R. Rajeev, J. Hellwagner, A. Schumacher, I. Jordan, M. Huppert, A. Tehlar, B. R. Niraghatam, D. Baykusheva, N. Lin, A. von Conta and H. J. Wörner, *Light Sci. Appl.*, 2016, **5**, e16170.
4 R. A. Taylor, T. Otanicar and G. Rosengarten, *Light Sci. Appl.*, 2012, **1**, e34.
5 X. Chen, C. Chardin, K. Makles, C. Caër, S. Chua, R. Braive, I. Robert-Philip, T. Briant, P. -F. Cohadon, A. Heidmann, T. Jacqmin and S. Deléglise, *Light Sci. Appl.*, 2017, **6**, e16190.
6 A. Emadi, H. Wu, G. de Graaf, P. Enoksson, J. H. Correia and R. Wolffenbuttel, *Appl. Opt.*, 2012, **51**, 4308.
7 T. J. Manning and D. Winefordner, *Rev. Sci. Instrum.*, 1990, **61(5)**, 1554.
8 C. Williams, G. Rughoobur, A. J. Flewitt and T. D. Wilkinson, *App. Opt.*, 2016, **55(32)**, 9237.
9 A. Emadi, H. Wu, S. Grabarnik, G. de Graff, K. Hedsten, P. Enoksson, J. H. Correia and R. F. Wolffenbuttel, *Sens. Actuators, A*, 2010, **162**, 400.
10 A. Piegari, J. Bulir and A. K. Sytchkova, *Appl. Opt.*, 2008, **47**, C151.
11 S. -W. Wang, X. Chen, W. Lu, L. Wang, Y. Wu and Z. Wang, *Opt. Lett.*, 2006, **31(3)**, 332.
12 B. E. Collins, K. -P. S. Dancil, G. Abbi and M. J. Sailor, *Adv. Funct. Mater.*, 2002, **12**, 187.
13 C. M. Thompson, M. Nieuwoudt, A. M. Ruminski, M. J. Sailor and G. M. Miskelly, *Langmuir*, 2010, **26**, 7598.
14 Y. Y. Li, P. Kim and M. J. Sailor, *Phys. Stat. Sol. (a)*, 2005, **202**, 1616.
15 C. M. Thompson, A. M. Ruminski, A. G. Sega, M. J. Sailor and G. M. Miskelly, *Langmuir*, 2011, **27**, 8967.
16 Y. L. Khung and N. H. Voelcker, *Opt. Mater.*, 2009, **32**, 234.
17 A. Santos, *J. Mater. Chem. C*, 2017, DOI: 10.1039/c6tc05555a.
18 W. Lee and J. S. Park, *Chem. Rev.*, 2014, **114**, 7487.
19 G. D. Sulka, *Highly Ordered Anodic Porous Alumina Formation by Self-Organized Anodizing* in Nanostructured Materials in Electrochemistry, Wiley-VCH Verlag Gmbh&Co. KGaA, 2008, 1-116 pp.
20 A. Santos, T. Kumeria and D. Losic, TrAC, *Trends Anal. Chem.*, 2013, **44**, 25.
21 A. Santos, T. Kumeria and D. Losic, *Materials*, 2014, **7**, 4297.
22 T. Kumeria, A. Santos and D. Losic, *Sensors*, 2014, **14**, 11878.
23 H. Masuda, M. Ohya, H. Asoh, M. Nakao, M. Nohtomi and T. Tamamura, Jpn. *J. Appl. Phys.*, 1999, **38**, L 1403.
24 H. Masuda, M. Ohya, K. Nishio, H. Asoh, M. Nakao, M. Nohtomi, A. Yokoo and T. Tamamura, *Jpn. J. Appl. Phys.*, 2000, **39**, L 1039.
25 H. Masuda, M. Ohya, H. Asoh and K. Nishio, *Jpn. J. Appl. Phys.*, 2001, **40**, L 1217.
26 Y. Chen, A. Santos, Y. Wang, T. Kumeria, C. Wang, J. Li and D. Losic, *Nanoscale*, 2015, **7**, 7770.
27 Y. Chen, A. Santos, Y. Wang, T. Kumeria, J. Li, C. Wang and D. Losic, *ACS Appl. Mater. Interfaces*, 2015, **7**, 19816.
28 Y. Chen, A. Santos, Y. Wang, T. Kumeria, D. Ho, J. Li, C. Wang and D. Losic, *Sci. Rep.*, 2015, **5**, 12893.
29 G. D. Sulka and K. Hnida, *Nanotechnology*, 2012, **23**, 075303.
30 J. Martín, M. Martín-González, J. F. Fernández and O. Caballero-Calero, *Nat. Commun.*, 2014, **5**, 5130.
31 B. Wang, G. T. Fei, M. Wang, M. G. Kong and L. D. Zhang, *Nanotechnology*, 2007, **18**, 365601.
32 W. J. Zheng, G. T. Fei, B. Wang, Z. Jin and L. D. Zhang, *Mater. Lett.*, 2009, **63**, 706.
33 W. J. Zheng, G. T. Fei, B. Wang and L. D. Zhang, *Nanoscale Res. Lett.*, 2009, **4**, 665.
34 A. Santos, T. Pereira, C. S. Law and D. Losic, *Nanoscale*, 2016, **8**, 14846.
35 A. Santos, C. S. Law, D. W. Chin Lei, T. Pereira and D. Losic, *Nanoscale*, 2016, **8**, 18360.
36 G. Macias, J. Ferré-Borrull, J. Pallarès and L. F. Marsal, *Nanoscale Res. Lett.*, 2014, **9**, 315.
37 P. -Y. Wang, L. R. Clements, H. Thissen, W. -B. Tsai and N. H. Voelcker, *Biomater. Sci.*, 2013, **1**, 924.
38 K. Kant, S. P. Low, A. Marshal, J. G. Shapter and D. Losic, *ACS Appl. Mater. Interfaces*, 2010, **2**, 3447.
39 A. Santos, J. H. Yoo, C. V. Rohatgi, T. Kumeria, Y. Wang and D. Losic, *Nanoscale*, 2016, **8**, 1360.
40 A. Santos, P. Formentín, J. Ferré-Borrull, J. Pallarès and L. F. Marsal, *Mater. Lett.*, 2012, **67**, 296.
41 Y. Wang, A. Santos, A. Evdokiou and D. Losic, *Electrochim. Acta*, 2015, **154**, 379.
42 M. D. Abràmoff, P. J. Magalhaes and S. J. Ram, *Biophotonics Int.*, 2004, **11**, 36.
43 A. Santos, V. S. Balderrama, M. Alba, P. Formentín, J. Ferré-Borrull, J. Pallarès and L. F. Marsal, *Adv. Mater.*, 2012, **24**, 1050.
44 A. Santos, T. Kumeria, Y. Wang and D. Losic, *Nanoscale*, 2014, **6**, 9991.
45 Y. Su, G. T. Fei, Y. Zhang, P. Yan, H. Li, G. L. Shang and L. D. Zhang, *Mater. Lett.*, 2011, **65**, 2693.
46 M. M. Rahman, L. F. Marsal, J. Pallarès and J. Ferré-Borrull, *ACS Appl. Mater. Interfaces*, 2013, **5**, 13375.
47 T. Kumeria, A. Santos, M. M. Rahman, J. Ferré-Borrull, L. F. Marsal and D. Losic, *ACS Photonics*, 2014, **1**, 1298.
48 C. S. Law, A. Santos, M. Nemati and D. Losic, *ACS Appl. Mater. Interfaces*, 2016, **8**, 13542.



 

View Article Online
DOI: 10.1039/C7NR02115A



49 Y. Wang, Y. Chen, T. Kumeria, F. Ding, A. Evdokiou, D. Losic and A. Santos, *ACS Appl. Mater. Interfaces*, 2015, **7**, 9879.
50 A. Santos, T. Kumeria and D. Losic, *Anal. Chem.*, 2013, **85**, 7904.